Applied Energy 395 (2025) 126180

Contents lists available at ScienceDirect

Applied Energy

journal homepage: www.elsevier.com/locate/apen

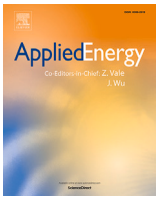

Numerical study of enhanced cooling in active elastocaloric regenerators with porous woven structures

Kun Wang, Manfred Kohl, Jingyuan Xu*

Institute of Microstructure Technology, Karlsruhe Institute of Technology, 76344, Karlsruhe, Germany

HIGHLIGHTS

- Active elastocaloric regenerators based on woven structures are proposed and investigated.
- A 1-D numerical model is developed to optimize the woven patterns and dimensions.
- A 30 % plain weave regenerator achieves a 11.3 W/g specific cooling power with a COP of 1.48 at 20 K.
- The cooling capacity of plain and twilled weave regenerators is improved significantly.

ARTICLE INFO

Keywords:
Elastocaloric cooling
1-D numerical model
Woven structure
Active elastocaloric regenerator

ABSTRACT

Elastocaloric cooling is an emerging solid-state technology that leverages the reversible latent heat of phase transformation in superelastic shape memory alloys to achieve efficient and environmentally friendly refrigeration. The performance of the regenerator, where elastocaloric effect and heat transfer occur, critically depends on the elastocaloric material and structural design. This study employs a 1-D numerical active elastocaloric regenerator model to evaluate the cooling performance of different woven-structure regenerators. Three typical woven structures—plain weave, twilled weave, and dutch weave—are investigated across varying porosities. The results indicate that a plain weave regenerator with 30 % porosity achieves the highest performance, delivering a maximum cooling power of 485 W, a specific cooling power of 11.3 W/g, and a COP of 1.48 under a 20 K temperature span. Twilled weave regenerators exhibit comparable performance, whereas dutch weave regenerators show significantly lower cooling capabilities. Both plain and twilled weave regenerators outperform the parallel plate regenerator, increasing cooling power by a factor of 3.3, due to enhanced heat transfer and specific heat transfer area. The study highlights the potential of woven-structure regenerators for high-performance elastocaloric cooling, offering insights into optimizing regenerator design and operational parameters while emphasizing their promise for efficient and sustainable solid-state cooling systems.

1. Introduction

Rising environmental and climate challenges necessitate urgent efforts to reduce greenhouse gas emissions [1]. Common volatile refrigerants used in vapor compression refrigeration, such as HydroFluoroCarbons (HFCs), have Global Warming Potentials (GWP) thousands of times greater than that of carbon dioxide, significantly exacerbating environmental issues [2]. Elastocaloric cooling has emerged as a promising and sustainable alternative to conventional vapor-compression refrigeration, leveraging solid-state elastocaloric materials (eCM) to eliminate the risk of hazardous gaseous refrigerant leaks.

Typical elastocaloric materials, such as superelastic Shape Memory Alloys (SMAs), exhibit a pronounced thermal response to mechanical stress due to the latent heat associated with phase transformations [3–5]. When uniaxial stress is applied to an SMA, its temperature increases as austenite transforms into martensite, releasing heat to surroundings. Conversely, when the stress is released, the SMA transforms back from martensite to austenite, absorbing heat from surroundings and causing a temperature drop. This reversible elastocaloric effect enables the construction of a thermodynamic cycle under cyclic stress, forming the basis for elastocaloric refrigeration.

* Corresponding author.
Email address: jingyuan.xu@kit.edu (J. Xu).

https://doi.org/10.1016/j.apenergy.2025.126180
Received 5 March 2025; Received in revised form 11 May 2025; Accepted 19 May 2025
Available online 29 May 2025

Nomenclature

Abbreviations

1-D	One dimensional
AER	Active elastocaloric regenerator
CHEX	Cold heat exchanger
eCE	Elastocaloric effect
eCM	Elastocaloric material
GWP	Global warming potential
HHEX	Hot heat exchanger
PP	Parallel plate
SMAs	Shape memory alloys

Symbols

A_c	Cross-section area [m^2]
C	Clausius–Clapeyron coefficient [–]
COP	Coefficient of performance [–]
c_p	Specific heat capacity [$J \cdot kg^{-1}K^{-1}$]
d	diameter [mm]
D_h	Hydraulic diameter [mm]
E_A	Elastic Young's modulus of the austenite [mm]
f	Frequency [Hz]
f_F	Friction factor [–]
Gz	Graetz number [–]
h	Convection heat transfer coefficient [$W \cdot m^{-2}K^{-1}$]
k	Thermal conductivity [$W \cdot m^{-1}K^{-1}$]
K	Coefficient of phase transformation temperatures [–]
L	Regenerator length [mm]
m	Mass [kg]
$\dot{m}$	Mass flow rate [$kg \cdot s^{-1}$]
M	Spacing of wires [mm]
Nt	The number of time nodes [–]
Nu	Nusselt number [–]
Nx	The number of spatial nodes [–]
ΔP	Pressure drop [Pa]
Q	Cooling/heating energy [J]
Pr	Prandtl number [–]
$\dot{Q}$	Cooling/heating power [W]
Re	Reynolds number [–]
S	Entropy [$J \cdot kg^{-1}K^{-1}$]
SCP	Specific cooling power [W/g]
t	Time [s]
T	Temperature [K]
ΔT	Temperature change [K]
T_{span}	Temperature span [K]
U	Utilization [–]
v_s	Superficial velocity (open velocity) [m/s]
V	Volume [m^3]
W	Work [J]
ϵ	Strain [–]
σ	Stress [MPa]
ρ	Density [$kg \cdot m^{-3}$]
Δ	Difference
τ	Period time [s]
ϵ	Porosity [–]
μ	Dynamic viscosity [s·Pa]

Subscripts and superscripts

ad	Adiabatic
AM	austenite transforming into martensite
amb	Ambient
c	Cold side, or cooling
disp	Dispersion
f	Fluid, or finish
h	Hot side
hys	Hysteresis
in	Inlet/inflow
iso	Isothermal
max	Maximum
min	Minimum
mech	Mechanical
out	Outlet/outflow
s	Solid, or start
stat	Static
tot	Total
tran	Transition
w	Wire

Recently, regenerative elastocaloric cooling prototypes, as illustrated in Fig. 1, have seen rapid development to achieve substantial temperature spans and cooling capacities. On the one hand, regenerative cooling enables temperature spans 2–4 times greater than the adiabatic temperature changes in the material under a large regeneration ratio, primarily due to the recycled heat generated by the regenerator and reduced losses [6–8]. On the other hand, the use of heat transfer fluids significantly enhances heat exchange efficiency compared to solid-to-solid heat contact [9–11]. The first regenerative elastocaloric heat pump device, developed by Tušek et al., utilized the tension of parallel NiTi plates and achieved a maximum temperature span of 19.9 K and a maximum specific heating power of 0.8 W/g [12]. Subsequent studies revealed that elastocaloric prototypes employing the compression of NiTi regenerators could achieve considerable fatigue life [13,14], which has now become the dominant approach in most prototypes [8,15,16]. Building on these advancements, further improvements in regenerative elastocaloric cooling systems have focused on enhancing heat exchange efficiency, with the regenerator's high specific surface area playing a key role. To address this, regenerators have been designed using thin-walled NiTi tubes or microchannel NiTi tubes, which provide significantly increased surface areas. For instance, Qian et al. developed a multi-mode elastocaloric cooling prototype that delivered a cooling power of 260 W and a temperature span of 22 K, utilizing NiTi tubes under compression modes [16]. Zhou et al. further optimized the regenerator geometry by incorporating grooved spiral channels inside tubular NiTi to achieve a high specific surface area of 7.8 cm^2/g. Their cascaded elastocaloric device achieves a cooling power of 203 W [11]. By employing multiple materials with different transition temperatures and improving the surface area of the regenerator to 12.5 cm^2/g, Zhou et al. extended the system's temperature lift to 75 K [8]. More recently, a kilowatt elastocaloric prototype utilizing parallelized tubular NiTi with a high specific surface area of 12.5 cm $^2/g$ has been demonstrated, marking a significant step toward the commercial application of elastocaloric heating and cooling [17].

While experimental prototypes offer valuable insights, numerical modeling of Active Elastocaloric Regenerators (AER) plays an equally essential role in advancing regenerative elastocaloric cooling systems. Achieving maximum cooling performance in regenerative elastocaloric systems requires careful optimization of regenerator structures, system design, and operating parameters. Numerical modeling of AER has proven to be a powerful tool for predicting system performance and guiding design improvements. This approach has been instrumental in

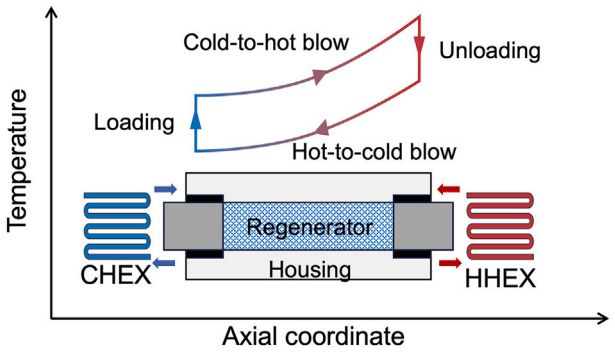

Fig. 1. Schematic of the operation of regenerative elastocaloric regenerators, illustrating four processes: *i* adiabatic loading, where the regenerator undergoes compression, leading to a temperature rise; *ii* cold-to-hot blow, with heat-transfer fluid flowing from the Cold Heat Exchanger (CHEX) to the Hot Heat Exchanger (HHEX) to transfer heat; *iii* adiabatic unloading, where the regenerator cools upon stress release, absorbing heat; *iv* hot-to-cold blow, with fluid flowing from HHEX to CHEX to complete the cycle. The cyclic operation of adiabatic compression, fluid flow, and stress release establishes a steady-state condition, producing a temperature span at a specific cooling load for elastocaloric refrigeration.

the development of advanced active caloric regenerators with various porous structures [10,18–23]. In earlier studies, Jaka et al. developed a 1-D numerical model for AERs based on NiTi alloys to evaluate the elastocaloric cooling performance of parallel plate NiTi regenerators [4]. Building on this, Ahin et al. improved the model by incorporating empirical correlations for the Nusselt number and friction factor specific to shell-and-tube-like elastocaloric regenerators, achieving a more accurate prediction for the regenerator performance [24,25]. Masselli et al. developed a numerical model for the development of check temperature, an active regenerator system based on bending and using air as heat transfer fluid [22]. Cirillo et al. developed a rotational model of a rotary air conditioner based on SMA-wire tension and convective heat exchange with water [26]. More recently, numerous emerging studies have focused on optimizing the structures of elastocaloric regenerators, such as foam structures and internal microchannel structures [27–29]. These investigations have provided critical insights into how structural variations impact performance, laying the groundwork for next-generation regenerator designs.

In this study, we propose a novel active elastocaloric regenerator design featuring porous woven structures and develop an advanced numerical model to simulate AERs with various woven configurations. The porous woven structures demonstrate significantly higher specific heat transfer areas compared to foam regenerator designs [27]—by a factor of 4.3 (under 50 % porosity)—showcasing their great potential for enhancing cooling performance. These woven structures are typically fabricated using two perpendicular sets of threads, the weft and the warp, interlaced with one another. This design allows for customization of mesh types, mesh sizes, and wire dimensions to achieve a high specific surface area, effectively addressing the demands for enhanced heat transfer performance. Thanks to these unique advantages, woven structures have been widely applied in efficient heat exchangers and regenerators across various technologies [30–34]. The improved heat transfer performance of porous woven structures highlights their strong potential for constructing high-performance elastocaloric regenerators, paving the way for further advancements in elastocaloric cooling technology.

2. Methodology

2.1. Experimental material characterization

The experimental material characterization is essential for constructing the dataset of the eCE under different temperatures and strains/stresses for numerical simulation. The eCE, which primarily includes the isothermal entropy change (ΔS_{iso}) and adiabatic temperature change (ΔT_{ad}), is evaluated based on the phenomenological model of superelasticity described in Section 2.2.

The NiTi wire used for material characterization is a commercial wire with a diameter of 151 μm and an initial length of 10 mm, sourced from Fort Wayne Metals. Mechanical test was performed on a Zwick tensile testing machine equipped with a 50 N load cell. The isothermal mechanical behavior was characterized using a custom temperature chamber, following the method described in [35]. The chamber's temperature was monitored with a T-type thermocouple, and mechanical tests were conducted once a stabilized temperature was reached. The isothermal tests were performed at temperatures of 298 K, 306 K, 314 K, 322 K, and 334 K. Prior to the test, the wire underwent training for 600 cycles at a strain rate of 0.002 s^{-1}. Training was conducted under stress control between 5 MPa and 498 MPa, as shown in Fig. 2(a). After training, the isothermal tests were conducted at a strain rate of 0.0002 s^{-1}. Fig. 2(b) shows the isothermal test results of the NiTi wire at various testings, which are subsequently utilized for phenomenological modeling in Section 2.2. The phase transformation temperatures of NiTi wires are measured by differential scanning calorimetry.

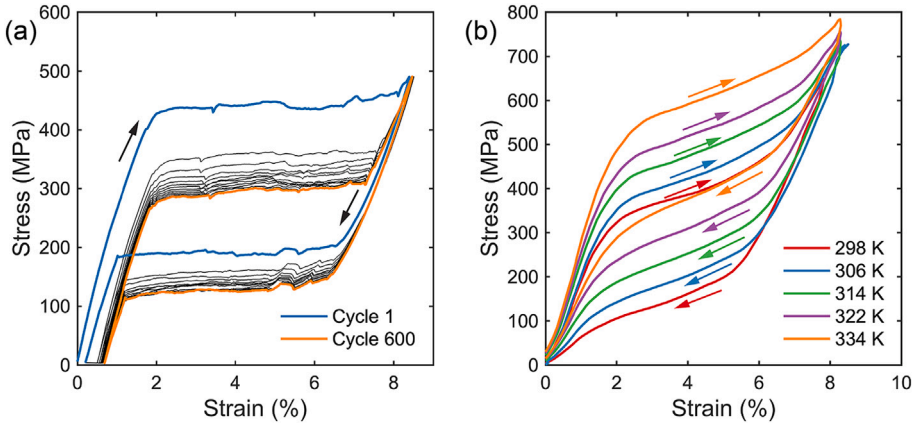

Fig. 2. Experimental mechanical behavior of NiTi wires: (a) NiTi wires underwent mechanical training for 600 cycles at 0.002 s^{-1} strain rate before isothermal testing (curves represent data sampled at 50-cycle intervals); (b) Temperature-dependent stress–strain profiles of NiTi wires under isothermal test at a strain rate of 0.0002 s^{-1}.

2.2. Phenomenological model for superelasticity

A phenomenological model is commonly used to extract the temperature-dependent superelastic behavior of SMAs as input for numerical modeling of AERs [36,37]. This model can be expressed as follows:

$$\varepsilon(\sigma,T)=\frac{\varepsilon_{\text{tran}}}{2}\tanh\left(\frac{K}{C_{\text{AM}}\left(M_s-M_f\right)}\cdot\left(\sigma-\sigma_{\text{AM}}(T)\right)\right)+\frac{\sigma}{E_{\text{A}}}+\frac{\varepsilon_{\text{tran}}}{2}, \tag{1}$$

This model describes the mechanical behavior during the phase transformation from austenite to martensite, i.e., the loading process. In this study, only the loading process is modeled to represent the superelastic behavior of the SMA, while the elastocaloric properties are subsequently adjusted using experimentally determined irreversibilities to account for hysteresis effects, similar to the method reported in elastocaloric simulations [25,38].

The isothermal entropy change of the eCM can be calculated using the Maxwell relation [39], based on the temperature-dependent superelastic behavior (i.e., temperature-dependent stress–strain profiles) derived from the phenomenological model:

$$\Delta S_{\text{iso}}=\frac{1}{\rho}\int_{\varepsilon_1}^{\varepsilon_2}\left(\frac{\partial\sigma}{\partial T}\right)_{\varepsilon}dT \tag{2}$$

The total entropy can be evaluated as the sum of the total entropy at zero strain and the isothermal entropy changes, minus half of the irreversible entropy ΔS_{hys} [25,40]:

$$S_{\text{tot}}(\varepsilon,T)=S_{tot,\varepsilon=0}+\Delta S_{\text{iso}}-\frac{\Delta S_{\text{hys}}}{2} \tag{3}$$

where the irreversible entropy, ΔS_{hys} (representing the hysteresis of the elastocaloric effect), can be determined from the hysteresis loop observed in stress–strain profiles:

$$\Delta S_{\text{hys}}=\Delta S_{\text{load}}-\Delta S_{\text{unload}}=\frac{1}{\rho T}\oint\varepsilon d\sigma, \tag{4}$$

According to the entropy-temperature profiles constructed by Eq. (3), the adiabatic temperature changes can be determined as follows:

$$\Delta T_{\text{ad}}=T_2\left(S_{\text{tot}},\varepsilon\right)-T_1\left(S_{\text{tot}},\varepsilon=0\right) \tag{5}$$

From the isothermal mechanical test described in Section 2.1, the required parameters for phenomenological modeling, including the elastic modulus of austenite phase (E_A), transition strain (ε_{tran}), Clausius–Clapeyron coefficient (C_{AM}), were obtained. These parameters are listed in Table 1, and the constant K using in the phenomenological model is 2.9444, as reported in literature [37]. The Clausius–Clapeyron coefficient, C_{AM}, which represents the transformation from austenite to martensite, was determined from the slope of the temperature-dependent critical stresses shown in Fig. 3(b).

Using the phenomenological model, the stress–strain profiles at different temperatures fit well for both the loading and unloading processes, as illustrated in Fig. 3(a). The mechanical behavior during the

Table 1
Parameters of NiTi wires using for the phenomenological model and eCE calculation, where the parameters K, density (ρ), and specific heat capacity (c_p) of NiTi is obtained from literature [37].

E_A (GPa)	ε_{tran}	K	C_{AM} (MPa/K)	M_s (K)	M_f (K)	M_p (K)	ρ (kg/m^3)	c_p (J/kgK)
23.8	0.049	2.9444	6.07	296	264	275	6500	430

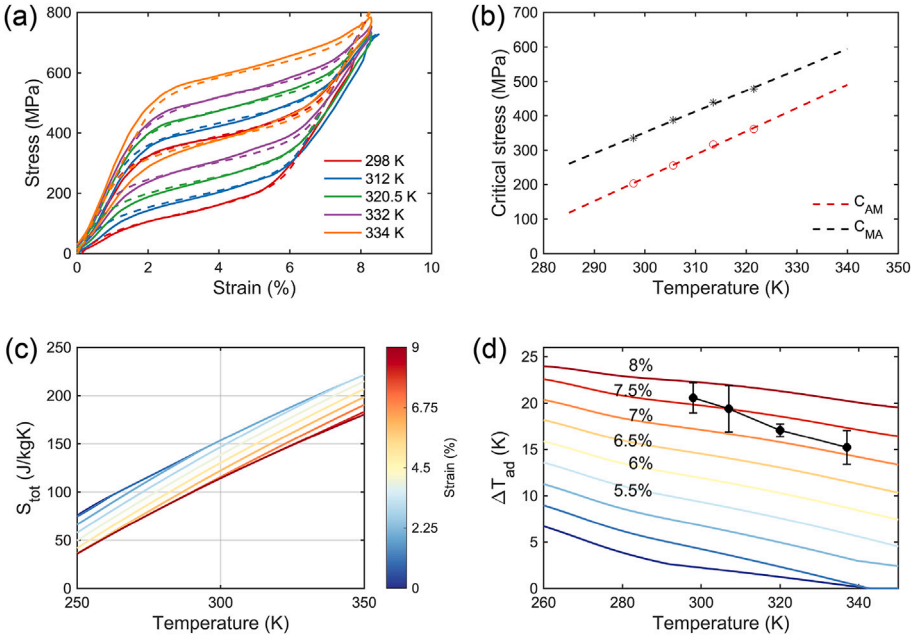

Fig. 3. Phenomenological modeling and eCE calculation and validation: (a) Fitting of isothermal stress–strain profiles using the phenomenological model, where solid lines represent experimental results and the dashed line represent model predictions; (b) Experimental temperature-dependent critical stress (dots) used to determine the Clausius–Clapeyron coefficient; (c) Calculated total entropy (S_{tot}) as a function of temperature under different strains; (d) Calculated adiabatic temperature changes (ΔT_{ad}) from $S_{tot}-T$ profiles, with the dark points representing experimental adiabatic temperature changes measured at 296 K under a strain of 8 % based on infrared thermography.

reverse transformation process can also be described by adapting Eq. (1), by modifying the Clausius–Clapeyron coefficient to account for the reverse transformation from martensite to austenite (C_{MA}), as detailed in [37]. For the baseline calculation of the total entropy as a function of temperature $S_{tot} - T$, the method was compared in reference [37], which recommends integrating the constant c_p with the isothermal entropy changes derived from the superelastic behavior of eCMs, rather than relying on calorimetry measurements. This is because R-phase transformation often shift the transformation temperature and alter the slope of the transformation lines. In this study, we adopted this method to calculate the baseline for $S_{tot} - T$ profiles using Eq. (3), as shown in Fig. 3(c). The specific heat capacity (c_p) of 430 J/kgK and the density of 6500 kg/m^3 for NiTi material, as reported in [37], were applied. Using Eq. (5), the adiabatic temperature changes as a function of temperature for NiTi wires were derived from the $S_{tot} - T$ curves. Fig. 3(d) compares the calculated ΔT_{ad} with experimental result at different temperatures (298, 307, 320, 337 K) under a strain of 8 %. At 298 K, the experimental ΔT_{ad} of 20.6 ± 1.63 K was slightly lower than the modeled value of 22.3 K at the same strain but showed a good agreement, consistent with previous findings in [4]. At higher temperatures, the discrepancy between the measured adiabatic temperature changes and the calculated values increases, which may be attributed to the thermal expansion of the material, and the initial length of the sample consequently expands. In the experiments, all samples were measured under the same engineering strain. The $S_{tot} - T$ profiles under different strains, obtained through phenomenological modeling of the material's superelasticity, will be used in the subsequent numerical modeling.

2.3. Geometry of regenerators and heat transfer correlations

To evaluate the potential of porous woven structures for regenerative elastocaloric cooling, simulations were conducted on three typical woven designs: plain weaves, twill weaves, and dutch weaves. A parallel plate (PP) structure was also simulated for comparison. Fig. 4 illustrates the geometries of the different regenerator beds within a single unit. The simulated regenerator has a cylindrical shape with a diameter of 10 mm and a length of 30 mm, constructed by stacking circular woven mesh units along the axial direction. In the simulation, it is assumed that the stacked layers are perfectly aligned without any angular displacement, and the fluid channels run parallel to each layer. For the parallel plate bed, the dimensions are defined by the plate thickness (H_1) and the spacing between the plates (H_2). The dimensions of the woven mesh beds are determined by the wire diameter (d_w) and the spacing between the wires (M), following the method presented by Armour and Cannon [41]. The calculated porosity and specific surface area for different regenerators structures are provided in Table 2.

Fig. 5 compares the porosity and specific surface area of various porous regenerator beds. For the parallel plate bed, the plate thickness is 0.1 mm. For the woven structures, the diameter of the wire used for weaving is also 0.1 mm. In this paper, the porosities of 30 %, 50 %, and 70 % for the woven structures were simulated, as listed in Table 6. The

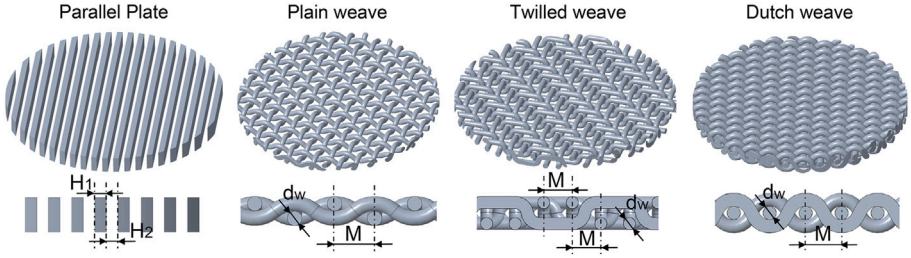

Fig. 4. Four different regenerator beds: parallel plate, plain weave, twilled weave, dutch weave.

Table 2
Calculation of the specific surface area (a_s) and porosity for four different types of regenerator beds. The formulas of the woven beds are adopted from [41].

Bed type	Dimension	Specific surface area, a_s	Porosity, ϵ
Parallel plate	H_1, H_2	$a_s = \frac{2}{H_1+H_2}$	$\epsilon = \frac{H_2}{H_1+H_2}$
Plain weave	d_w, M	$a_s = \frac{\pi}{M^2}\sqrt{d_w^2+M^2}$	$\epsilon = 1 - \frac{\pi d_w}{4M^2}\sqrt{d_w^2+M^2}$
Twilled weave	d_w, M	$a_s = \frac{\pi}{2M^2}\left(\sqrt{d_w^2+M^2}+M\right)$	$\epsilon = 1 - \frac{\pi d_w}{8M^2}\left(\sqrt{d_w^2+M^2}+M\right)$
Dutch weave	d_w, M	$a_s = \frac{\pi}{3M^2}\left(\sqrt{4d_w^2+M^2}+M\right)$	$\epsilon = 1 - \frac{\pi d_w}{6M^2}\left(\sqrt{4d_w^2+M^2}+M\right)$

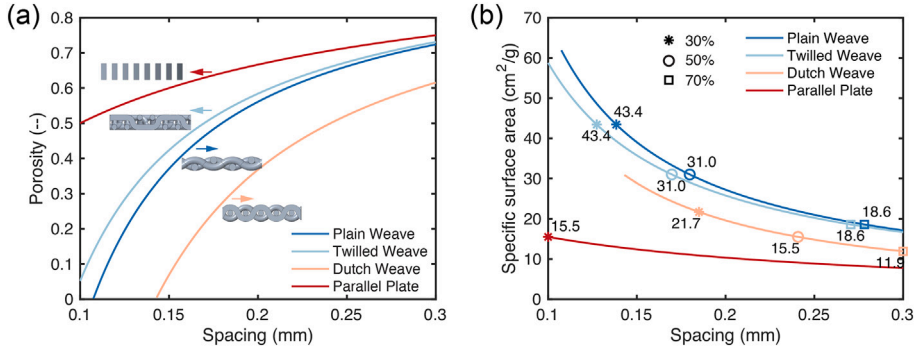

Fig. 5. Porosity (ϵ) and specific surface area (a_s) as functions of the spacing between weaving wires or plates. The wire diameter for the woven structures is 100 μm, and the plate thickness for the parallel plate beds is also 100 μm.

corresponding specific surface areas under these porosities are denoted in Fig. 5(b) using different points. The porosity and specific surface area can be effective controlled by adjusting the spacing between the plates or wires. Interestingly, the plain weave exhibits a significantly superior specific surface area (31.0 cm^2/g), twofold higher than that of the parallel plate beds (15.5 cm^2/g) under an identical porosity of 50 %. The other two woven structures, twill and dutch weaves, also demonstrate high specific surface area. The twilled weave reaches an equivalent specific surface area as the plain weave when both have identical porosity. As reported in elastocaloric prototypes [11], a higher surface area enhances heat transfer, leading to improved temperature span and specific cooling power. This suggests that employing these woven structures holds great promise for achieving enhanced cooling performance.

The correlation of heat transfer parameters is crucial for accurately modeling porous active elastocaloric regenerators (AERs) operating with aqueous heat transfer fluids. In most studies on active magnetocaloric regenerators, such correlations are typically established under low Reynolds numbers ($Re < 100$) [10,42,43]. Two key parameters that require correlation in the AER model are the pressure drop (ΔP), which accounts for viscous dissipation, and the Nusselt number (Nu), which represents heat transfer between the solid and fluid phases. The pressure drop can be calculated using the friction factor (f_F), a dimensionless parameter dependent on the Reynolds number. Table 3 compares various methods for calculating the friction factor for different AER beds. Among these, the friction correlations proposed by Armour and Cannon offer a more suitable estimation for this study [41], as they were derived for porosities in the range of 0.35–0.759. In contrast, the correlations in [44,45] were developed for regenerators with porosities above 0.7, which may introduce deviations in this study. For dutch weave beds, the friction correlation developed by Liu et al. [46] is applied. The pressure drop is generally expressed as a function of the friction factor:

$$\Delta P = f_F L \frac{\rho_f \left(\frac{v_s}{\epsilon}\right)^2}{2D_h} \tag{6}$$

where L, v_s, ϵ, and D_h represent the length of the regenerator, superficial velocity, porosity, and hydraulic diameter, respectively. For packed woven beds, D_h is calculated using the relation between porosity and specific surface area for the woven structure regenerator: $D_h = \frac{4\epsilon}{a_s}$ [10]. For the parallel plate regenerator, $D_h = 2H_2$ is used, as described in [47].

The Nusselt number (Nu) and Reynolds number (Re) can be calculated as follows:

$$\begin{aligned} \mathrm{Nu} &= \frac{hD_h}{k_f} \\ \mathrm{Re} &= \frac{\rho_f v_s D_h}{\mu_f} \end{aligned} \tag{7}$$

where ρ_f, D_h, μ_f, h, k_f, and v_s represent the density of the heat transfer fluids, hydraulic diameter, dynamic viscosity, heat transfer coefficient, thermal conductivity of the fluids, and open velocity of the fluids, respectively. The calculation of the Nusselt number for different regenerator bed types are provided in Table 4.

2.4. Numerical model for active elastocaloric regenerators

A 1-D numerical model for elastocaloric regenerator was developed, adapted from models used for active magnetocaloric regenerators [54,55]. The governing equations are as follows:

$$\begin{aligned} A_c \epsilon \rho_f c_f \frac{\partial T_f}{\partial t} = \frac{Nuk_f}{D_h} a_s A_c \left(T_s - T_f\right) + \frac{\partial}{\partial x}\left(k_{disp} A_c \frac{\partial T_f}{\partial x}\right) \\ - \dot{m}_f c_f \frac{\partial T_f}{\partial x} + \left|\frac{\partial P}{\partial x}\frac{\dot{m}_f}{\rho_f}\right| \end{aligned} \tag{8}$$

$$\begin{aligned} \frac{\partial T_s}{\partial t} = \frac{Nuk_f a_s}{D_h \rho_s c_s (1-\epsilon)}\left(T_f - T_s\right) + \frac{1}{\rho_s c_s (1-\epsilon)}\frac{\partial}{\partial x}\left(k_{stat}\frac{\partial T_s}{\partial x}\right) \\ + \frac{T_s}{c_s}\left(\frac{\partial S}{\partial \epsilon}\right)_T \frac{\partial \epsilon}{\partial t} + \frac{T_s}{c_s}\Delta S_{hys}\left|\frac{\partial \epsilon}{\partial t}\right| \end{aligned} \tag{9}$$

where T_s and T_f are the solid and fluid temperatures, x is the axial coordinate (along the regenerator length), and ϵ is the porosity. A_c is the cross-section area, k_{disp} and k_{stat} represent the thermal conductivity of fluid dispersion and static thermal conductivity, respectively, $\dot{m}_f$ is the mass flow rate of the fluid, and a_s is the specific surface area of the regenerator. The subscripts s and f denote parameters corresponding to the

Table 3
Pressure drop and friction factor correlations for different regenerator bed types.

Woven types	Reference	Friction factor	Pressure drop	Remarks
Parallel plate	Bejan [48]	$f_F = \frac{64}{Re}$ $Re = \frac{\rho_f(\frac{v_s}{\epsilon})D_h}{\mu_f}$	$\frac{dP}{dx} = f_F\left[\frac{\rho_f(\frac{v_s}{\epsilon})^2}{2D_h}\right]$	Laminar flow
Plain weave	Armour et al. [41]	$f_F = \frac{8.61}{Re} + 0.52$ $Re = \frac{\rho_f(\frac{v_s}{\epsilon})D_h}{\mu_f}$	$\frac{dP}{dx} = f_F\left[\frac{\rho_f(\frac{v_s}{\epsilon})^2}{D_h}\right]$	Re = 0.1–1000
	Tanaka et al. [44]	$f_F = \frac{175}{\mathrm{Re}} + 1.6$ $Re = \frac{\rho_f(\frac{v_s}{\epsilon})D_h}{\mu_f}$	$\frac{dP}{dx} = f_F\left[\frac{\rho_f(\frac{v_s}{\epsilon})^2}{D_h}\right]$	Re = 0.1–1000,
	Wu et al. [45]	$f_F = 250\frac{1-\epsilon}{\mathrm{Re}} + 1.69\left(\frac{1-\epsilon}{\mathrm{Re}}\right)^{0.071}$ $Re = \frac{\rho_f(\frac{v_s}{\epsilon})D_h}{\mu_f}(1-\epsilon)$	$\frac{dP}{dx} = f_F\left[\frac{\rho_f(\frac{v_s}{\epsilon})^2}{D_h}\right]$	Re = 85–12,000, ϵ = 0.602–0.919
Twilled weave	Armour et al. [41]	$f_F = \frac{8.61}{Re} + 0.52$ $Re = \frac{\rho_f(\frac{v_s}{\epsilon})D_h}{\mu_f}$	$\frac{dP}{dx} = f_F\left[\frac{\rho_f(\frac{v_s}{\epsilon})^2}{D_h}\right]$	Re = 0.1–1000
	Wu et al. [45]	$f_F = 206.5\frac{1-\epsilon}{\mathrm{Re}} + 2.14\left(\frac{1-\epsilon}{\mathrm{Re}}\right)^{0.071}$ $Re = \frac{\rho_f(\frac{v_s}{\epsilon})D_h}{\mu_f}(1-\epsilon)$	$\frac{dP}{dx} = f_F\left[\frac{\rho_f(\frac{v_s}{\epsilon})^2}{D_h}\right]$	Re = 85–12,000, ϵ = 0.602–0.919
Dutch weave	Wu et al. [45]	$f_F = 182.2\frac{1-\epsilon}{\mathrm{Re}} + 3.54\left(\frac{1-\epsilon}{\mathrm{Re}}\right)^{0.071}$ $Re = \frac{\rho_f(\frac{v_s}{\epsilon})D_h}{\mu_f}(1-\epsilon)$	$\frac{dP}{dx} = f_F\left[\frac{\rho_f(\frac{v_s}{\epsilon})^2}{D_h}\right]$	Re = 85–12,000, ϵ = 0.602–0.919
	Liu et al. [46]	$f_F = \frac{56.9}{Re} + 4.08$ $Re = \frac{\rho_f(\frac{v_s}{\epsilon})D_h}{\mu_f}$	$\frac{dP}{dx} = f_F\left[\frac{\rho_f(\frac{v_s}{\epsilon})^2}{D_h}\right]$	Re = 2–65

Table 4
Empirical correlations for Nusselt number in various regenerator bed configurations.

Woven types	Reference	Nusselt number	Remarks
Parallel plate	Nickolay et al. [47]	$\mathrm{Nu} = \left[7.541^n + \left(1.841Gz^{1/3}\right)^n\right]^{(1/n)}$ $\mathrm{Gz} = \frac{2v_s A_{cof} c_C D_L}{k_f W_p L}$, $n = 3.592$	$\mathrm{Gz} < 10^5$
Plain weave	Park et al. [49]	$Nu = 1.315Pr^{1/3}Re^{0.35}\left(\frac{1-\epsilon}{\epsilon}\right)^{0.2}$ $Re = \frac{\rho_f\left(\frac{v_s}{\epsilon}\right)D_h}{\mu_f}$	Re = 10–500
	Yang et al. [50]	$Nu = 0.76Pr^{0.37}Re^{0.4}$	Re = 0–40
	Kolodziej et al. [51]	$Nu = \frac{2\left[(4/\pi)\cdot L^*\right]^{-1/2}}{\left[1+(F)/0{,}0207)^{2/8}\right]^{1/4}}\left(0270\cdot(\mathrm{Pr}\cdot L^*)^{-0213}\right)$ $L^* = \frac{L}{D_h \mathrm{RePr}} = \frac{\pi}{4}\frac{1}{Gz}$	Re = 2–300 Gz = 2.5–1960
Twilled weave	Bin-Nun et al. [52]	$Nu = (1 + 0.99Pe^{0.66})\epsilon^{1.79}$ $Pe = RePr$	Laminate flow
Dutch weave	Yang et al. [53]	$Nu = 0.971Pe^{0.969}$, $Pe = RePr$	Re = 0.01–10, Pr = 1.27–5.86
	Liu et al. [46]	$Nu = 0.06Re^{0.69}Pr^{1/3}\epsilon^{0.70}$	Re = 2–65

solid matrix (regenerator materials) and the heat-transfer fluid, respectively. The hysteresis of entropy, ΔS_{hys}, is introduced into the model as an entropy generation term and reformulated into Eq. (9), following the approach outlined in [38]. The hysteresis ΔS_{hys} has been calculated as 2.05 J/kgK, which is 5 % of the maximum entropy change 40.62 J/kgK of the NiTi material obtained under a strain of 7 %.

In this simulation, the woven regenerators are modeled by stacking the woven layers shown in Fig. 4 under compression. When these woven structures are stacked at different angles, such as having an angle between different layers, the stress distribution within the regenerator during compression may become non-uniform. The misalignment and deformation of the flow channels cause the fluid flow direction distorted, resulting in an increased pressure drop. During operation, the regenerator undergoes cyclic loading and unloading, while also experiencing heat exchange with the surrounding housing and loading head. The use of insulating materials can reduce this heat loss. To simplify the model, the regenerator is considered as a uniform stack of multiple layers of woven structures, with well-aligned fluid channels. During compression, the stress distribution in the regenerator is uniform. The deformation during the loading and unloading processes is reversible. As a result, the following assumptions are applied for the simulation of the woven regenerators: (1) The stress throughout the regenerator is homogeneous. (2) The heat transfer fluid is incompressible. (3) The fluid channels in the woven meshes are perfectly aligned between the stack layers. (4) The deformation and buckling of the mesh under compression are neglected. (5) The strain can be fully recovered with 100 % work recovery. (6) The strain remains constant during the fluid flow period. (7) Heat transfer between the regenerator and the housing or load heads is neglected. (8) The heat transfer fluid flows perpendicular to the bed unit, along the regenerator length. (9) The effect of fluid tortuosity in complex dutch weaves is neglected. (10) The material data obtained from tensile tests can approximate the elastocaloric effect (eCE) of the material under compression tests.

Among these assumptions, assumptions one and ten are critical to the validity of the simulated results. For the first assumption, stress was assumed to be homogeneous throughout the woven regenerator. This assumption is based on the symmetrical design of the woven regenerator (cylindrical shape) and the operating conditions (fast loading and load holding), which promote an even distribution of mechanical load. While intrinsic local stress concentrations exist at microscale features during the compression of woven regenerators, our primary aim is to model the macroscopic behavior of the system, where stress homogeneity provides a reasonable and simplifying assumption. The effect of stress inhomogeneity at microscale can be analyzed based on finite element simulation for 3D woven structure and used to evaluate the fraction of stress uniformity across the woven regenerator [56]. For the assumption 10, we assumed the use of tensile data to approximate the elastocaloric effect (eCE) of compression data. There are two key factors to justify this: (1) symmetry of eCE at high strains associated with ΔT_{ad} and (2) hysteresis of tension and compression associated with COP_{mat}, which are justified carefully in Supplementary Note 1.

In the simulation, the governing equations were discretized using central difference and implicit time integration schemes for both spatial and temporal domains, as described in [57]. The discretization employed 100 spatial nodes ($N_x = 100$) and 2500 temporal nodes ($N_t = 2500$). The model evaluates performance indices upon reaching thermal steady-state conditions within a specified tolerance of 10^{-5}. The time step (Δt) of simulation is obtained from a period of the elastocaloric cycle (τ) divided by the number of temporal node (N_t):

$$\Delta t = \tau / N_t \tag{10}$$

To estimate if calculation reaches cyclic thermal equilibrium, the evolution of cooling power and COP with time is given in Supplementary Fig. 1 for a 50 % plain weave regenerator under a utilization of 2.38 at 2 Hz with a 20 K temperature span. In this 1-D model, the temperature difference between the heat sink (T_h) and heat source (T_c) is set as the boundary condition by defining different operation temperature spans. With an increase in iterations, when the calculation error converges to a value lower than the target error the calculation is terminated, and the steady state is reached. The governing equations were formulated into a matrix equation and solved using MATLAB software.

The performance of an Active Elastocaloric Regenerator (AER) is influenced by various operational parameters, including operating frequency (f), applied strain (ε), working temperature (T_H), mass flow rate ($\dot{m}_f$) or utilization (U), and the geometries of the regenerator, such as porosity (ϵ) and channel dimension (e.g., wire spacing or plate spacing for woven and parallel plate structures). The working temperature refers to the temperature of the hot reservoir or the hot exchanger for cooling implementation. Utilization is a dimensionless parameter that represents the ratio of the thermal mass of the heat transfer medium displaced per blow to that of the regenerator solid. It is directly associated with the mass flow rate ($\dot{m}_f$) [58], and is defined as:

$$U = \frac{\int_0^{\tau/2} \dot{m}_f c_f dt}{m_s c_s} = \frac{V_{\mathrm{pump}} \rho_f c_f}{m_s c_s} \tag{11}$$

The mass flow rate of the fluid can be defined as:

$$\dot{m}_f = \rho_f v_s A_c \tag{12}$$

The performance of an AER, once steady state conditions are reached, can be assessed using several key parameters, including temperature span, cooling power, specific cooling power, and Coefficient of Performance (COP). The temperature span is calculated as the difference between the average outlet temperatures at the hot side (T_h) and the cold side (T_c) of the regenerator.

$$T_{span} = T_h - T_c \tag{13}$$

The cooling power ($\dot{Q}_c$) and Specific Cooling Power (SCP) of the regenerator are defined as:

$$\dot{Q}_c = f \int_0^{\tau} \dot{m}_f c_f \left(T_{f,c,\text{out}} - T_{f,c,\text{in}}\right) dt. \tag{14}$$

$$SCP = \frac{f}{m_s} \int_0^{\tau} \dot{m}_f c_f \left(T_{f,c,\text{out}} - T_{f,c,\text{in}}\right) dt. \tag{15}$$

The coefficient of performance of the regenerator is calculated as the ratio of the cooling energy (Q_c) to the total input work, which includes the mechanical work (W_{mech}) required to drive the elastocaloric regenerator and the pump work (W_{pump}) for fluid flow:

$$COP = \frac{Q_c}{W_{mech} + W_{pump}} \tag{16}$$

The cooling energy, mechanical work and pump work are defined as:

$$\begin{aligned} Q_c &= \int_0^{\tau} \dot{m}_f c_f \left(T_{f,c,\text{out}} - T_{f,c,\text{in}}\right) dt, \\ W_{\text{mech}} &= V_s \oint \sigma d\varepsilon, \\ W_{\text{pump}} &= \int_0^{\tau} \frac{\dot{m}_f \cdot \Delta P}{\rho_f} dt. \end{aligned} \tag{17}$$

where V_s is the volume of the regenerator, and ΔP is the pressure drop of the fluid flow across the hot and cold sides of the regenerator, see the details of ΔP calculation in Supplementary Note 2.

Table 5 presents the main operating parameters used in the numerical simulation, while Table 6 provides the geometrical information of the different regenerator beds used. The four different regenerator configurations are designed with identical dimensions but varying porosities to compare their performance. This ensures that regenerators with the same porosity have equivalent mass. For regenerators with woven structures, the effect of porosity on performance is investigated. These woven regenerators are fabricated using wires of the same diameter but with varying spacings to achieve different porosities. The objective of the numerical modeling in this study is to determine the optimal cooling capacity and coefficient of performance of the regenerators under varying operating frequencies and mass flow rates. In the simulation, the hot side temperature is fixed at 300 K, and a 7 % applied strain is used, as it corresponds to the end of the phase transformation of NiTi wires, as observed in Fig. 2(a).

Table 5
Parameters used in the numerical modeling of porous elastocaloric regenerators. The table specifies the geometries, materials, fluids, and operational parameters employed in the simulations.

Parameters	Value
Regenerator geometries	Parallel plate matrix Plain weave matrix Twilled weave matrix Dutch weave matrix
Regenerator material	NiTi
Heat transfer fluids	Water
Thermal conductivity of solid, k_s [$Wm^{-1}K^{-1}$]	10
Thermal conductivity of fluid, k_f [$Wm^{-1}K^{-1}$]	0.56
Maximum applied strain, ϵ [%]	7
Total regenerator length, L [mm]	30
Regenerator diameter, d [mm]	10
Hot-side temperature, T_h [K]	300
Ambient temperature, T_{amb} [K]	296
Temperature span, T_{span} [K]	10, 20, 30, 40
Operating frequency, f [Hz]	0.2, 0.5, 0.8, 1.0, 1.5, 2
Hysteresis, $\Delta S_{hys}/\Delta S_{iso,\max}$ [%]	5

Table 6
Geometrical parameters of different regenerator bed configurations used in the simulation.

Regenerator beds	Parallel plate	Plain weave	Twilled weave	Dutch weave
L [mm]	30	30	30	30
H_1 [μm]	100	\	\	\
d_w [μm]	\	100	100	100
H_2 [μm]	100	\	\	\
M [μm]	\	138, 180, 292	170, 271	241, 373
ϵ [–]	0.5	0.3, 0.5, 0.7	0.3, 0.5, 0.7	0.3, 0.5, 0.7
m_s [g]	30.6	49.2, 30.6, 18.4	49.2, 30.6, 18.4	49.2, 30.6, 18.4

3. Results and discussion

3.1. Optimization of operating frequency and utilization

The maximum cooling power and coefficient of performance of a regenerator are strongly influenced by the operating frequency and mass flow rate of the heat transfer fluid. Therefore, the elastocaloric performance as a function of utilization (which is related to mass flow rate) is analyzed under varying operating frequencies for different regenerators.

Fig. 6 illustrates the elastocaloric performance of a plain weave regenerator with a porosity of 0.5. Fig. 6(a) and (b) show the results simulated at a temperature span of 20 K, while Fig. 6(c) and (d) correspond to a temperature span of 40 K. For the plain weave regenerator, both cooling power and COP initially increase with utilization, reach a peak, and then decline, indicating an optimal utilization point for each operating frequency. Additionally, higher operating frequencies lead to a significant increase in cooling power. Compared to a parallel plate regenerator operated under identical conditions with a temperature span of 40 K, as shown in Fig. 7, the plain weave regenerator achieves a maximum cooling power of 243 W at a utilization of 2.03 at 2 Hz. This value is significantly higher than the maximum cooling power of 73 W ($U = 1.75, f = 1$ Hz) observed in the parallel plate regenerator in Fig. 7. Under 30 K temperature span, the parallel plate regenerator with optimal utilization achieves a maximum specific cooling power of 3.22 W/g (see in Fig. 8), which is comparable to the 3.1 W/g reported for a modeled parallel plate regenerator operating at 1 Hz [59]. In our simulation, the parallel plate regenerator serves as a benchmark for comparison with woven-structure regenerators, as we conducted an experimental validation based on a parallel plate regenerator (see Supplementary Note 3 and Supplementary Fig. 6). The enhanced cooling performance in the plain weave regenerator is resulting from its higher specific surface area compared to the PP regenerator—by a factor of 2 (50 % porosity), which improves heat transfer between the regenerator and the fluids. Interestingly, the COP of the plain weave regenerator is comparable to that of the parallel plate regenerator under the same 40 K temperature span, indicates a similar efficiency. However, it is worth noting that for the parallel plate regenerator under a 40 K temperature span, the maximum cooling power decreases as the operating frequency increases, suggesting an optimal operating frequency at 1 Hz.

3.2. Impact of porosity on cooling performance

The influence of porosity on the cooling performance of various regenerators can be explored by analyzing the maximum cooling power, specific cooling power, and COP, obtained at optimal utilization, as functions of operating frequency. Fig. 8(a) compares the maximum cooling power and SCP of plain weave regenerators with porosities of 30 %, 50 %, and 70 % to that of a parallel plate regenerator with 50 % porosity under a temperature span of 20 K. The results indicate that the maximum cooling power of plain weave regenerators increases with operating frequency, consistent with trends reported for NiTi tubular prototypes [11].

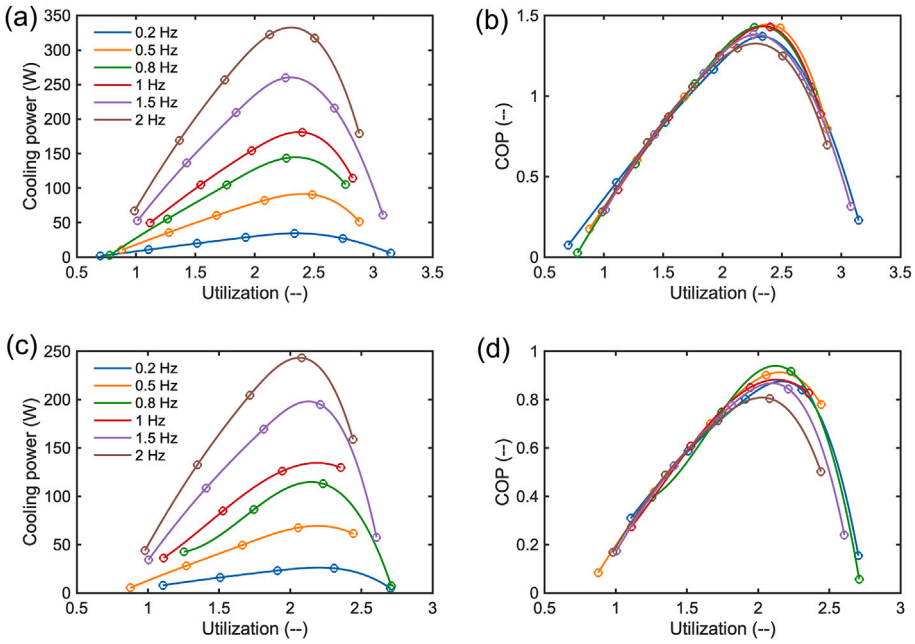

Fig. 6. Effect of utilization and operating frequency on cooling power and COP of plain weave regenerator ($\epsilon = 0.5$), (a) and (b) obtained at a temperature span of 20 K, (c) and (d) obtained at a temperature span of 40 K.

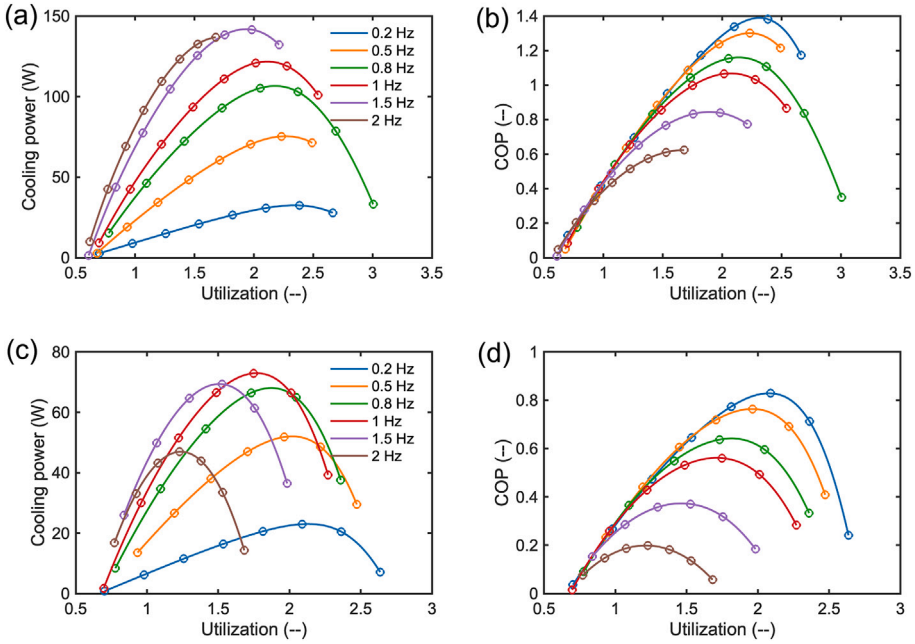

Fig. 7. Effect of utilization and operating frequency on cooling power and COP of parallel plate regenerator ($\epsilon = 0.5$), (a) and (b) obtained at a temperature span of 20 K, (c) and (d) obtained at a temperature span of 40 K.

However, as porosity increases, the cooling power decreases significantly, while the SCP shows only a minimal reduction. For example, at 2 Hz, the maximum cooling power of the plain weave regenerator decreases from 485 W at 30 % porosity to 195 W at 70 % porosity, representing nearly a 50 % reduction. Meanwhile, the SCP exhibits a slight decline, from 11.3 W/g to 10.6 W/g. This behavior is attributed to the change in the regenerator's thermal mass, which significantly influences the cooling power as porosity varies. The higher cooling power observed in the 30 % porosity regenerator is attributed to its larger regenerator mass of 49.2 g, which is substantially greater than the 18.4 g of the 70 % porosity regenerator. Conversely, the cooling power of the 50 % parallel plate regenerator does not increase monotonically with frequency; instead, it begins to decline when the frequency exceeds 1.5 Hz. Notably, when the frequency is above 0.2 Hz, the maximum cooling power of the plain weave regenerator surpasses that of the parallel plate regenerator. For instance, at 2 Hz, the 50 % plain weave regenerator achieves a cooling power of 333 W—nearly 2.5 times higher than the 137 W produced by the parallel plate regenerator, despite having the same regenerator mass. This highlights the superior suitability of the plain weave regenerator for operation at higher frequencies, offering significantly enhanced

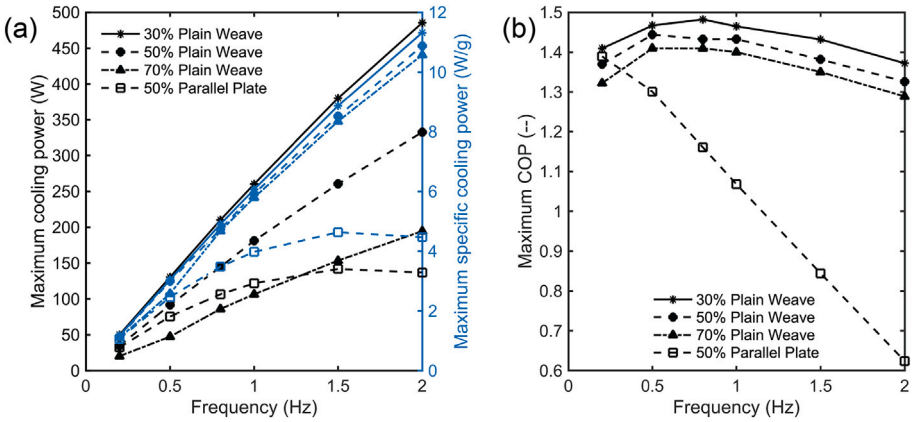

Fig. 8. Comparison of plain weave regenerators with different porosities (30 %, 50 %, 70 %) and a parallel plate regenerator (50 % porosity) at a temperature span of 20 K: (a) maximum cooling power (black) and maximum specific cooling power (blue), (b) maximum COP, based on optimized utilization for each configuration.

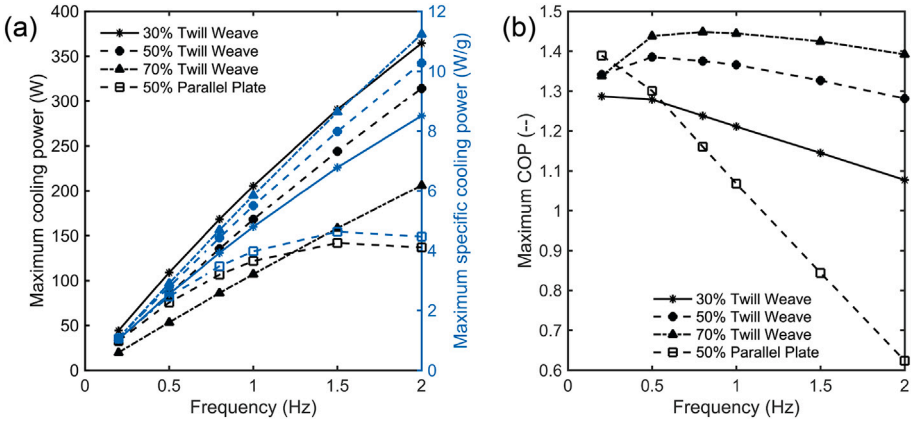

Fig. 9. Comparison of twilled weave regenerators with different porosities (30 %, 50 %, 70 %) and a parallel plate regenerator (50 % porosity) at a temperature span of 20 K: (a) maximum cooling power (black) and maximum specific cooling power (blue), (b) maximum COP, based on optimized utilization for each configuration.

cooling capacity. Additionally, the maximum COP of the plain weave regenerator exhibits a slight decline as frequency increases, reaching a peak of 1.48 observed at 0.8 Hz. In contrast, the maximum COP of the parallel plate regenerator shows a more pronounced reduction with frequency increase.

Similar to Figs. 8, 9 illustrates a comparison of the cooling performance of twilled weave regenerators to a 50 % parallel plate regenerator across various operating frequencies. The maximum cooling power of the twilled weave regenerators follows a similar trend with frequency and porosity, where higher porosity results in a significant reduction in cooling performance. Interestingly, the SCP of the twilled weave regenerator increases as porosity decreases. However, higher porosity improves the COP of the twilled weave regenerators see Supplementary Fig. 4. This improvement in COP can be attributed to the reduced pressure drop caused by increased porosity, which lowers the pump work contribution to the total input energy, as observed in Supplementary Fig. 4. For instance, at a frequency of 2 Hz and a utilization of 2, the pressure drops for regenerators with 30 %, 50 %, and 70 % porosities are 5.17 bar, 0.32 bar, and 0.02 bar, respectively. The fraction of pump power to total input power decreases from 1.38 % to 0.02 %, when porosity changes from 30 % to 70 %. Overall, the cooling performance of the twilled weave regenerators surpasses that of the parallel plate regenerator. For instance, at 2 Hz, the 50 % twilled weave regenerator achieves a maximum cooling power of 314 W, significantly higher than the 137 W produced by the parallel plate regenerator.

The cooling performance of the dutch weave regenerator, shown in Fig. 10, is compared to that of the parallel plate regenerator under a 20 K temperature span. Overall, its cooling performance is lower than that of the parallel plate regenerator. The maximum cooling power of dutch weave regenerators is 14.8 W, achieved with a 70 % porosity regenerator at 0.8 Hz, which is significantly lower than the 137 W achieved by the parallel plate regenerator. Unlike the twilled weave and plain weave regenerators, the cooling performance of dutch weave regenerators improves as porosity increases. This trend may be attributed to the dense structure of the dutch weave, which is formed by three interwoven strands [46], compared to the two interwoven strand sets in the other weaving types. At a same porosity of 50 %, the Dutch weave regenerator has a specific surface area of 15.5 cm^2/g, which is only half the specific surface area of the plain weave regenerator (31.0 cm^2/g). When the porosity is too low, the compact nature of the dutch weave restricts the vertical flow of the heat transfer fluid, reducing heat convection efficiency and resulting in poorer cooling performance and pronounced pressure drops. However, as the porosity increases to an optimal level, the improved flow rate and heat transfer efficiency slightly enhance the cooling performance.

When comparing the three woven structure regenerators, the plain weave regenerator demonstrates the best overall cooling performance. The twilled weave regenerator also exhibits a comparable maximum cooling power of 314 W, which is close to the 333 W achieved by the 50 % plain weave regenerator at 2 Hz. Additionally, the maximum COP achieved by the 70 % twilled weave regenerator surpasses that of

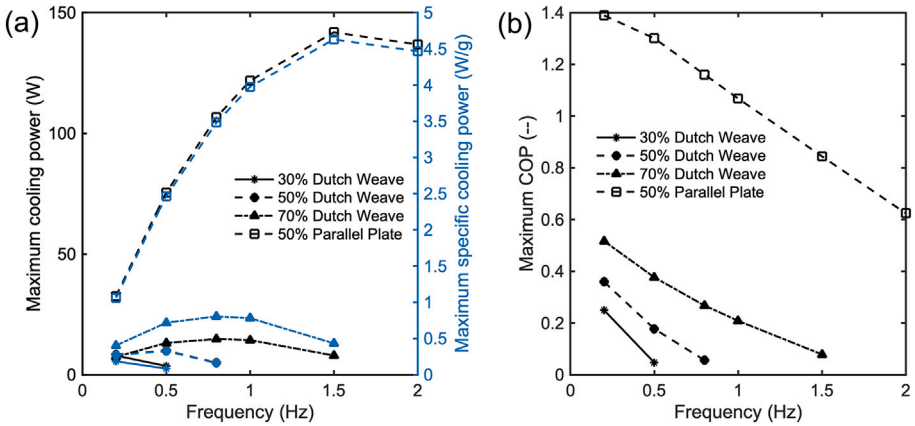

Fig. 10. Comparison of dutch weave regenerators with different porosities (30 %, 50 %, 70 %) and a parallel plate regenerator (50 % porosity) at a temperature span of 20 K: (a) maximum cooling power (black) and maximum specific cooling power (blue), (b) maximum COP, based on optimized utilization for each configuration.

the plain weave regenerator. These findings suggest that regenerators with plain weave and twilled weave structures hold significant potential for regenerative elastocaloric cooling, offering excellent cooling performance and high efficiency.

3.3. Impact of hysteresis on cooling performance

Hysteresis is an inherent characteristic of first-order transition caloric materials, manifesting as thermal and field hysteresis effects, which can significantly reduce the caloric effect of these materials [60,61]. At the prototype level, hysteresis in caloric materials degrades system performance due to the input work associated with hysteresis and the internal energy dissipation within the material. As reported in studies on elastocaloric regenerators [25,38], hysteresis can negatively affect regenerator performance during a cooling cycle, making it a critical factor in determining cooling performance when modeling AERs. In numerical models of active regenerators, hysteresis is typically evaluated as the difference between the positive entropy change during the application of the external field and the negative entropy change during its removal. Alternatively, hysteresis can be quantified using isothermal hysteresis loops and calculated with Eq. (4), which is then incorporated as an entropy generation term in the numerical model.

In this section, we examine the impact of hysteresis on cooling performance in a 50 % plain weave regenerator, operating with a 40 K temperature span under a 7 % strain. Fig. 11(a) and (b) present the maximum cooling power and COP, after optimization of utilization, as functions of the hysteresis reduction ratio at different operating frequencies. Here, 100 % hysteresis reduction represents zero hysteresis in the modeling, while 0 % hysteresis reduction corresponds to the complete hysteresis entropy obtained from the hysteresis loops used in the numerical model (the aforementioned simulations were all based on this approach). From the profiles of maximum cooling power and hysteresis reduction, it is evident that cooling power improves as hysteresis decreases. This effect is particularly pronounced at higher operating frequencies above 1 Hz. For example, at 2 Hz, the cooling power increases significantly from 243 W to 321 W as hysteresis is reduced from 0 to 100 %. However, at lower operating frequencies, such as 0.2 Hz and 0.5 Hz, hysteresis has a relatively minor influence on cooling capacity. This observation is consistent with simulated results from tube-based AERs operating at 0.5 Hz [25]. In the plain weave regenerator operating under a 40 K temperature span, hysteresis notably influences the COP of the cooling system across all operating frequencies, as shown in Fig. 11(b). For example, at 1 Hz, the COP increases more than twofold, from 0.88 to 2.64, when hysteresis reduction changes from 0 % to 100 %. This highlights the significant impact of hysteresis on regenerator cooling efficiency. For the other regenerator beds, the cooling performance follows a similar trend as the plain weave regenerator with the hysteresis reduction. To achieve efficient elastocaloric cooling with plain weave regenerators, NiTi wire with lower hysteresis is recommended to improve efficiency, but this often results in reduced latent heat, requiring a careful trade-off between cooling capacity and efficiency.

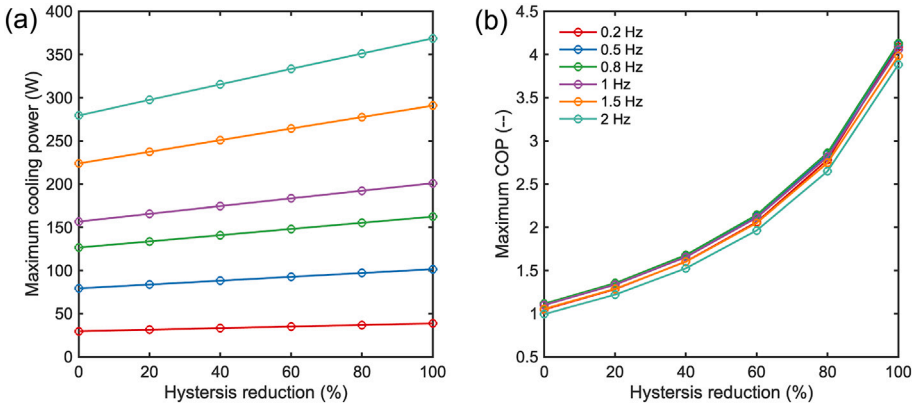

Fig. 11. Effect of hysteresis reduction ratio on a 50 % plain weave regenerator under different operating frequencies. (a) Maximum cooling power and (b) Maximum COP as functions of hysteresis reduction.

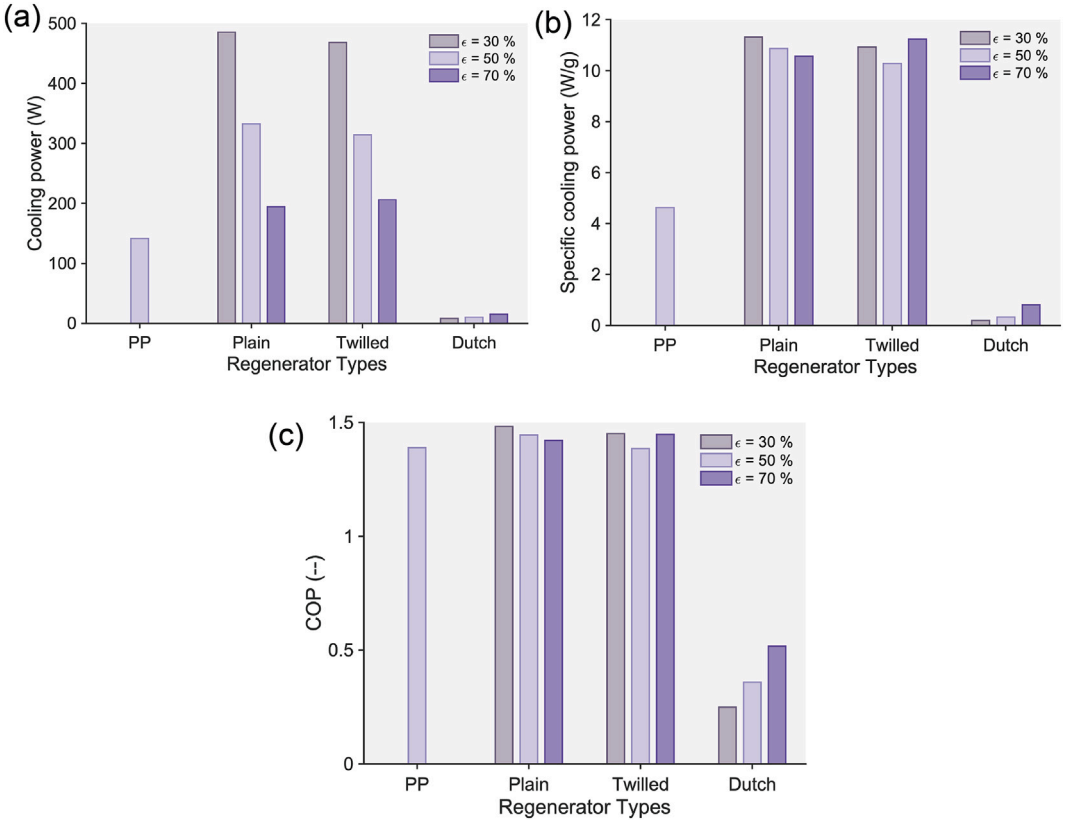

Fig. 12. Performance comparison of different regenerator beds across different porosities ϵ at a 20 K temperature span: (a) maximum cooling power, (b) specific cooling power (SCP), and (c) coefficient of performance (COP). These performance metrics are obtained under their optimal utilization and frequency. The abbreviation PP represents the parallel plate matrix.

3.4. Comparison of different woven structure regenerators

Here, we summarize the maximum cooling performance of different regenerators under their optimum utilization and frequency to evaluate their potential for elastocaloric cooling systems, as illustrated in Fig. 12. To obtain the maximum performance metrics of different regenerators, the operation frequency and utilization are both optimized for each performance metric. Fig. 12(a) and (b) present the maximum cooling power and specific cooling power of four types of regenerator beds operating under optimum conditions at a temperature range of 20 K. The maximum cooling power of 485 W is achieved with a $\epsilon = 30$ % plain weave regenerator at an optimal utilization of 1.6 and operating frequency of 2 Hz. At a porosity of $\epsilon = 50$ %, the plain weave and twilled weave regenerators deliver significantly higher cooling power, exceeding 300 W, compared to the 141 W obtained with the parallel plate regenerator. In terms of SCP, the $\epsilon = 70$ % twilled weave regenerator achieves 11.2 W/g, which is comparable to 11.3 W/g of the $\epsilon = 30$ % plain weave regenerator. For the twilled weave regenerator, higher porosity improves SCP, while for the plain weave regenerator, lower porosity enhances both cooling power and SCP. The SCP values for the plain weave and twilled weave regenerators are more than double the 4.63 W/g SCP of the parallel plate regenerator. This performance in parallel plate regenerator is comparable to the 4.1 W/g SCP achieved in simulations for NiTi-tube-based regenerators [62,63], which is significantly lower than the maximum SCP around 11 W/g achieved in plain weave and twilled weave regenerators (see Fig. 12(b)). The $\epsilon = 70$ % twilled weave regenerator, using 18.4 g of NiTi material, achieves an impressive SCP of 11.2 W/g, far surpassing the 1.25 W/g maximum SCP modeled in five elastocaloric regenerator designs with NiTi tubular structures [29] and 2.03 W/g SCP from the simulations of shell-and-tube regenerators [64]. Despite its lighter weight, the twilled weave regenerator delivers a cooling power of 206 W, higher than the 105 W of the shell-and-tube regenerator with 51.7 g NiTi alloys [64], showcasing its superior SCP.

It is important to note that discrepancies between simulation and experimental results are typical, as simulations are based on idealized assumptions regarding experimental conditions and regenerator geometry, which are discussed in detail in Section 4. Nevertheless, when compared to the parallel plate structure, the two woven-structure regenerators consistently exhibit superior cooling performance due to their enhanced heat transfer characteristics.

The maximum cooling efficiency parameter, COP, achieved in these regenerators, is compared in Fig. 12(c), and the best COP values, along with their corresponding optimal operating parameters—frequency f and utilization U—are summarized in Table 7. The highest COP of 1.48 is obtained with a $\epsilon = 30$ % plain weave regenerator, exceeding the 1.39 COP achieved with a $\epsilon = 50$ % parallel plate regenerator. This indicates that the plain weave regenerator, despite having a denser structure, delivers a higher cooling efficiency comparable to the parallel plate configuration. Additionally, regenerators with parallel plate, plain weave, and twilled weave beds exhibit similar COP values of approximately 1.4, showing minimal dependence on porosity. In contrast, the maximum COP of 0.52 observed in the dutch weave regenerator is significantly lower than that of the other regenerator types. The results suggest that plain weave and twilled weave regenerators are the most promising candidates for elastocaloric cooling applications, as they offer superior performance in terms of both specific cooling power and energy efficiency.

To estimate uncertainties in simulated cooling performance, we quantified uncertainties in simulated cooling power and COP for a

Table 7
The best COP of different regenerator beds, along with corresponding optimal utilization (U) and frequency (f), at a temperature span of 20 K.

Geometry	Porosity, ϵ	Utilization, U	Frequency, f (Hz)	COP
Parallel plate	0.5	2.31	0.2	1.39
Plain weaves	0.3	1.59	0.8	1.48
	0.5	2.38	0.5	1.44
	0.7	4.03	0.5	1.42
Twilled weaves	0.3	1.59	0.8	1.45
	0.5	2.35	0.5	1.39
	0.7	4.10	0.8	1.45
Dutch weaves	0.3	1.28	0.2	0.25
	0.5	1.90	0.2	0.36
	0.7	3.42	0.2	0.52

plain weave regenerator (50 %) by varying critical material properties (±5%): mass density caused ±4.3% cooling power shifts with minimal COP changes (±0.3%), thermal conductivity had negligible impact (< ±0.03% cooling power, ±0.11% COP), and applied strain, which is associated with adiabatic temperature changes, dominated deviations (±6–7% cooling power, inversely shifting COP by ±0.8–1.6%). Strain adjustments revealed a critical trade-off—higher strain boosts cooling power but reduces efficiency, while lower strain modestly improves COP at the cost of cooling power. Combined ±5% parameter variations amplified uncertainties (±10.5% cooling power, ±1.5% COP), as shown in Supplementary Fig. 7.

4. Conclusion

This study investigates the potential of woven-structure elastocaloric regenerators to achieve high-performance elastocaloric cooling using a 1-D numerical active elastocaloric regenerator model. The model effectively predicts key performance metrics, including cooling capacity, Specific Cooling Power (SCP), and Coefficient of Performance (COP), while optimizing critical operating parameters such as frequency and utilization. These findings provide valuable insights into selecting regenerator geometries and determining optimal operating conditions to enhance elastocaloric cooling system performance. The temperature-dependent superelastic behavior of NiTi wire is modeled using a phenomenological approach based on experimental data and integrated into the numerical simulation. Additionally, the hysteresis of the elastocaloric material is incorporated to reflect the practical performance of elastocaloric materials in regenerators. The impact of hysteresis on regenerator performance is also evaluated.

Among the simulated woven structures, the plain weave regenerator with 30 % porosity achieves a maximum cooling power of 485 W, an SCP of 11.32 W/g, and a COP of 1.48 under a 20 K temperature span. The twilled weave regenerator with higher porosity demonstrates comparable SCP and COP to the plain weave, while the dutch weave regenerator exhibits the lowest performance. These findings emphasize the promise of plain and twilled weaves for regenerative elastocaloric cooling due to their excellent specific surface areas and enhanced heat transfer capabilities.

While the study provides valuable insights, there is room for improvement in the current model to enhance prediction accuracy. The regenerator is modeled as a stack of woven-structure layers, assuming perfectly aligned microchannels within each layer and uniform applied stress throughout the structure during loading and unloading. However, in practice, misalignment of the woven layers during assembly can lead to nonuniform stress distribution, affecting the pressure drop and heat transfer coefficient under real operating conditions. To improve the model's accuracy, it is essential to incorporate experimental data for thermal-hydraulic properties of actual woven AERs. Combining these experimental data enables precise correlations for heat transfer performance and pressure drop, as demonstrated in previous studies [24,42]. Updating the model with such experimental information would significantly enhance its ability to predict the real-world performance of elastocaloric regenerators. Additionally, the assumption of uniform stress distribution and the neglect of local buckling across woven regenerators may overestimate/underestimate local strain variations, impacting eCE predictions, which causes simulation uncertainties in cooling power. In our future work, introducing a factor of stress uniformity across the woven regenerator based on finite element simulations can reduce this effect.

CRediT authorship contribution statement

Kun Wang: Writing – original draft, Visualization, Validation, Software, Investigation, Formal analysis, Data curation. **Manfred Kohl:** Writing – review & editing, Validation, Resources, Data curation. **Jingyuan Xu:** Writing – review & editing, Supervision, Project administration, Methodology, Funding acquisition, Conceptualization.

Declaration of competing interest

The authors declare that they have no known competing financial interests or personal relationships that could have appeared to influence the work reported in this paper.

Acknowledgments

The authors gratefully acknowledge the support provided by the Carl-Zeiss-Stiftung, the Baden-Württemberg Stiftung, the Hector Fellow Academy, and the Klaus Tschira Stiftung.

Supplementary data

Supplementary data to this article can be found online at doi:10.1016/j.apenergy.2025.126180.

Data availability

Data will be made available upon request.

References

[1] Dowling P. Energy Policy 2013;60:406–17.
[2] Kauffeld M. International Institute of Refrigeration, Paris; 2016. p. 1–15.
[3] Qian S, Geng Y, Wang Y, Ling J, Hwang Y, Radermacher R, et al. Int J Refrig 2016;64:1–19.
[4] Tušek J, Engelbrecht K, Millán-Solsona R, Manosa L, Vives E, Mikkelsen LP, et al. Adv Energy Mater 2015;5:1500361.
[5] Bruederlin F, Bumke L, Chluba C, Ossmer H, Quandt E, Kohl M. Energy Technol 2018;6:1588–604.
[6] Masche M, Liang J, Engelbrecht K, Bahl CRH. Appl Therm Eng 2022;204:117947.
[7] Chen Y, Wang Y, Sun W, Qian S, Liu J. The Innovation 2022;3.
[8] Zhou G, Li Z, Wang Q, Zhu Y, Hua P, Yao S, et al. Nat Energy 2024:1–9.
[9] Radebaugh R, Louie B. A simple, first step to the optimization of regenerator geometry. In: Proc. of the 3rd cryocooler conf.; 1985.
[10] Lei T, Engelbrecht K, Nielsen KK, Veje CT. Appl Therm Eng 2017;111:1232–43.
[11] Zhou G, Zhu Y, Yao S, Sun Q. Joule 2023;7:2003–15.
[12] Tušek J, Engelbrecht K, Eriksen D, Dall'Olio S, Tušek J, Pryds N. Nat Energy 2016;1:1–6.
[13] Chen J, Zhang K, Kan Q, Yin H, Sun Q. Appl Phys Lett 2019;115.
[14] Tušek J, Žerovnik A, Čebron M, Brojan M, Žužek B, Engelbrecht K, et al. Acta Mater 2018;150:295–307.
[15] Ahčin Ž, Dall'Olio S, ŽerovnikAndrej, Baškovič UŽ, Porenta L, Kabirifar P, et al. Joule 2022;6:2338–57.
[16] Qian S, Catalini D, Muehlbauer J, Liu B, Mevada H, Hou H, et al. Science 2023;380:722–27.
[17] Zhou G, Zhang L, Li Z, Hua P, Sun Q, Yao S. Nature 2025:1–6.
[18] Bouchard J, Nesreddine H, Galanis N. Int J Heat Mass Transfer 2009;52:1223–29.
[19] Liang J, Engelbrecht K, Nielsen KK, Loewe K, Vieyra H, Barcza A, et al. Appl Therm Eng 2021;186:116519.
[20] Qian S, Wang Y, Xu S, Chen Y, Yuan L, Yu J. Appl Energy 2021;298:117269.
[21] Kang M, Elbel S. Appl Therm Eng 2023;230:120769.
[22] Masselli C, Cirillo L, Greco A. Appl Therm Eng 2023;230:120729.
[23] Welsch F, Kirsch S-M, Michaelis N, Motzki P, Schmidt M, Schütze A, et al. Elastocaloric cooling: system design, simulation, and realization. In: Smart materials, adaptive structures and intelligent systems; vol. 51951. American Society of Mechanical Engineers; 2018. p. V002T08A005.
[24] Ahčin Ž, Liang J, Engelbrecht K, Tušek J. Appl Therm Eng 2021;190:116842.
[25] Ahčin Ž, Kabirifar P, Porenta L, Brojan M, Tušek J. Energies 2022;15:9253.

[26] Cirillo L, Greco A, Masselli C. Appl Therm Eng 2023;228:120487.
[27] Wu Y, Liu Y, Qian S. Appl Therm Eng 2023;221:119819.
[28] Zhu Y, Hur J, Cheng S, Sun Q, Li W, Yao S. Int J Heat Mass Transfer 2021;176:121372.
[29] Zhu Y, Zhou G, Cheng S, Sun Q, Yao S. Appl Energy 2023;339:120990.
[30] Kurian R, Balaji C, Venkateshan SP. Appl Therm Eng 2016;108:1158–67.
[31] Costa S-C, Tutar M, Barreno I, Esnaola J-A, Barrutia H, García D, et al. Energy 2014;72:800–12.
[32] Chen S, Huang Q, Liang M, Chen H, Chen L, Hou Y. Cryogenics 2018;96:99–107.
[33] Xu J, Hu J, Hu J, Zhang L, Luo E, Gao B. Cryogenics 2018;95:69–75.
[34] Chen G, Xu J. Appl Therm Eng 2022;213:118667.
[35] Tušek J, Engelbrecht K, Mikkelsen LP, Pryds N. J Appl Phys 2015;117.
[36] Tanaka K. Res Mech 1986;18:251–63.
[37] Tušek J, Engelbrecht K, Mañosa L, Vives E, Pryds N. Shape Mem Superelast 2016;2:317–29.
[38] Masche M, Ianniciello L, Tušek J, Engelbrecht K. Int J Refrig 2021;121:302–12.
[39] Bonnot E, Romero R, Mañosa L, Vives E, Planes A. Phys Rev Lett 2008;100:125901.
[40] Brey W, Nellis G, Klein S. Int J Refrig 2014;47:85–97.
[41] Armour JC, Cannon JN. AlChE J 1968;14:415–20.
[42] Liang J, Masche M, Engelbrecht K, Nielsen KK, Vieyra HA, Barcza A, et al. Appl Therm Eng 2021;197:117383.
[43] Engelbrecht K, Nielsen KK, Pryds N. Int J Refrig 2011;34:1817–22.
[44] Tanaka M, Yamashita I, Chisaka F. JSME Int J Ser 2 Fluids Eng Heat Transf Power Combust Thermophys Prop 1990;33:283–89.
[45] Wu WT, Liu JF, Li WJ, Hsieh WH. Int J Heat Mass Transfer 2005;48:3008–17.
[46] Liu Y, Xu G, Luo X, Li H, Ma J. Appl Therm Eng 2015;80:118–26.
[47] Nickolay M, Martin H. Int J Heat Mass Transfer 2002;45:3263–66.
[48] Bejan A. Entropy generation minimization: the method of thermodynamic optimization of finite-size systems and finite-time processes. CRC Press; 2013.
[49] Park J-W, Ruch D, Wirtz R. Thermal/fluid characteristics of isotropic plain-weave screen laminates as heat exchange surfaces. In: 40th AIAA aerospace sciences meeting & exhibit; 2002. p. 208.
[50] Zhu Q, Guo W, Zhuan R, Zhang P. Int J Heat Mass Transfer 2022;183:122208.
[51] Kołodziej A, Łojewska J, Jaroszyński M, Gancarczyk A, Jodłowski P. Int J Heat Fluid Flow 2012;33:101–08.
[52] Bin-Nun U, Manitakos D. Cryogenics 2004;44:439–44.
[53] Yang G, Xu R, Wang Y, Zhu Y, Ren F, Li C, et al. Chem Eng Sci 2022;256:117696.
[54] Nielsen KK, Tusek J, Engelbrecht K, Schopfer S, Kitanovski A, Bahl CRH, et al. Int J Refrig 2011;34:603–16.
[55] Lei T, Nielsen KK, Engelbrecht K, Bahl CR, Neves Bez H, Veje CT. J Appl Phys 2015;118.
[56] Lee MG, Lee KW, Hur HK, Kang KJ. Compos Struct 2013;95:264–77.
[57] Engelbrecht K, Bahl CRH. J Appl Phys 2010;108.
[58] Nielsen KK, Bahl CRH, Smith A, Pryds N, Hattel J. Int J Refrig 2010;33:753–64.
[59] Tušek J, Engelbrecht K, Pryds N. Sci Technol Built Environ 2016;22:489–99.
[60] Gutfleisch O, Gottschall T, Fries M, Benke D, Radulov I, Skokov KP, et al. Phil Trans R Soc A Math Phys Eng Sci 2016;374:20150308.
[61] Wu Y, Ertekin E, Sehitoglu H. Acta Mater 2017;135:158–76.
[62] Huang C, Liang J, Liu Z, Li T. Appl Phys Lett 2022;121.
[63] Qian S, Yuan L, Yu J, Yan G. Energy 2017;141:744–56.
[64] Ahčin Ž, Tušek J. Appl Therm Eng 2023;231:120996.